Journal of Energy and Natural Resource Management (JENRM), Vol. 10, No. 1, 31-39, 2024
Received: January 2, 2024; Revised: March 25, 2024; Accepted: April 18, 2024

Synthesis and characterization of metal oxides nanoparticles from metal-oleates single source precursors

Albright Boachie-Ameyaw[1,2*]; Selina Ama Saah[3]; Michael Baah Mensah[4]; Paul Ofori Amanfo[3]; James Kwabena Osei[2]

Abstract
Metal oxides nanoparticles resulting from the thermal decomposition of the oleate complex precursors have attracted the attention of many researchers in recent times, because of the distinct properties by virtue of their small size. The focus of this work was to synthesise and characterise ZnO, CuO and Fe_2O_3 nanoparticles through thermal decomposition of metal oleate complex, serving as a single-source precursor in a reactor (Melt Method). This method is effective, inexpensive, and high-quality crystalline structures are formed. Moreover, it presents several advantages. The purities of the precursors were confirmed by micro-elemental analyses and FT-IR. The decomposition pattern of the metal-oleate complexes were analysed with TGA and the images obtained were consistent with what have been reported in literature. The FT-IR showed the expected peaks that corresponds to Cu-O, Zn-O and Fe-O stretches. TEM images showed well-crystalline CuO nanoparticles with cubic symmetry and the calculated particle size of 8.2 nm from the XRD peaks. Similarly, the as-synthesised ZnO and Fe_2O_3 nanoparticles were characterized by XRD and the calculated particle sizes from the Debye Scherer equation were 11, and 16 nm respectively.

Keywords
Metal Oleate; Single-Source Precursors; Nanoparticles; Thermal Decomposition; Morphology

[1]Department of Environmental Management, University of Energy and Natural Resources, Sunyani, Ghana
[2]Department of Science, Berekum College of Education, Berekum, Ghana
[3]Department of Chemistry, University of Energy and Natural Resources, Sunyani, Ghana
[4]Department of Chemistry, Kwame Nkrumah University of Science and Technology, Kumasi, Ghana
***Corresponding author**: albrihgt@gmail.com

DOI: 10.26796/jenrm.v10i1.254
Received: January 2, 2024; **Received in revised form:** March 25, 2024; **Accepted:** April 18, 2024; **Published:** April 30, 2024

Contents

1. Introduction

Metal oxide nanoparticles have recently emerged as promising prospects for a variety of industrial and medicinal applications due to their distinct physical and chemical characteristics as compared to bulk materials. The utilization of organometallic complexes in the production of metal oxide nanoparticles, which are utilized to manufacture a variety of innovative materials, is receiving more attention (Niloufar and Abouzar 2019; Nikolova and Chavali, 2020). Similarly, due to their smaller size, metal oxide nanoparticles exhibit greater novelty and increased characteristics in terms of chemical, mechanical, and biological aspects (Sharma et al., 2019). Metal oxide nanoparticles are used as catalysts, gas sensors, sulfactants, opto-electronics, superconductors, and other applications owing to their unique properties. Furthermore, they are quite valuable in terms of anticancer measurement (Abbasi et al., 2018; Chavali and Nikolova, 2019).

Two fundamental ways are widely designed to create nanoparticles;(1) top-down approach where the preparation protocol is initiated with the bulk structure system leaching out methodologically bit-after-bit resulting to the formation of viable nanoparticles. This method of producing nanoparticles encompasses photolithography, electron beam lithography, milling processes, anodization, ion and plasma itching; and (2) bottom-up approach which includes the fusion of particles or assembly of atoms and molecules to form a varied spectrum of nanoparticles (Christian and Bogdan 2020). Self -assembly of monomer/polymer molecules, chemical or electrochemical nanomaterial precipitation, sol-gel processing, laser pyrosis, chemical vapour deposition, plasma or flame spraying synthesis and bio-assisted synthesis are examples of bottom-up approach (Christian and Bogdan 2020; Boles et al., 2016).

The goal of this research was to synthesis and analyse metal oxides (CuO, FeO, and ZnO) nanoparticles from single source metal-oleate precursors using a solventless approach and by thermally breaking down the precursors in a reactor (Melt method). A good precursor choice allows you to modify the characteristics of materials, which has an impact on the nature and form of the desired nanoparticles. It can readily be used as a building block to transform molecules into nanomaterials in one step (Parsa et al., 2021). In terms of the synthesis of metal oxides, metals, and metal chalcogenides nanoparticles, solventless breakdown of a single source precursor looks to be a highly promising technique (Chen et al., 2007; George et al., 2018). This approach is effective, inexpensive, quick, and has less toxicity restrictions. Furthermore, there is no need for a capping agent, and the instrumental setup is simple. The interactions between metal salts and sodium oleate complex produced zinc, copper, and iron oleates complexes. The resulting metal oxide nanoparticles namely ZnO, CuO, and Fe_2O_3 which would be synthesized, will be subjected to several characterization methods, such as TGA, FT-IR, XRD, TEM, and micro-elemental analysis.

2. Materials and methods

All the analytical reagents employed in this study were of the highest quality and did not need to be purified further. The chemicals were purchased from Sigma Aldrich(South Africa) and local vendors.

2.1 Synthesis of metal oleate complex precursor

Generally, metal-oleate complexes can be synthesised by the reaction between metal oleate, ethanol, hexane, and salt of the metal.

2.2 Synthesis of Iron oleate complex precursor

During the synthesis of the iron oleate complex, 4 mmol of $FeCl_3\ .6H_2O$ (96 %) and 12 mmol of sodium oleate (98 %) were dissolved in a mixture consisting of 8 mL of ethanol (98.9 %), 6 mL distilled water and 14 mL hexane (96 %). The resulting mixture was heated for 4 hours at a constant temperature of 70 ^oC. After the 4 hours an upper organic layer containing the iron oleate complex was formed. It was washed three times with distilled water using solvent extraction procedure in a separating funnel. Hexane was evaporated off after washing. The resulting product, iron oleate complex appeared as dark orange solid.

2.3 Synthesis of Zinc oleate complex precursor

The synthesis of zinc oleate complex involved, dissolving of 4 mmol of Zn $(CH_3COO)_2\ .2H_2O$ (97 %) and 8 mmol of sodium oleate in a mixture composing of 8 mL ethanol, 6 mL distilled water and 14 mL hexane. The solution that resulted was heated up to a temperature of 70 ^oC for 4 hours. The upper organic layer containing the zinc oleate complex was washed three times with distilled water in a separating funnel. After washing, hexane was evaporated off and it resulted in the formation of zinc oleate complex with a white waxy solid.

2.4 Synthesis of Copper oleate complex precursor

Copper oleate complex was synthesised in a similar fashion. 4 mmol $\mathrm{CuCI_2.2H_2O}$ (99 %) and 8 mmol of sodium oleate were dissolved in a mixture consisting of 8 mL ethanol, 6 mL distilled water and 14 mL hexane. The solution formed was heated to 70 ^oC for 4 hours. The upper organic layer that contained copper oleate complex was washed three times with distilled water in a separating funnel. After washing, hexane was evaporated off, resulting in the formation of copper oleate complex solid which was a waxy in nature and looked greenish blue.

2.5 Characterization of metal oleate precursors

The thermal and chemical properties of the as-synthesised metal oleate precursors were determined and compared to literature.

2.6 Fourier Transform-Infrared Spectroscopy (FT-IR)

Perkin Elmer FT-IR spectrophotometer with Bruker detector was used to obtain the IR spectra. The samples were scanned as solids from 4000 - 500 cm^{-1}. Wave numbers of the spectra were compared to literature to determine the different functional groups in the sample. Some of the limitations associated with FTIR analysis include interference distortion within the film, reflection distortions at the boundary with the cell window, only specific inorganic species exhibits FTIR spectra among others.

2.7 Micro-Elemental Analysis (MEA)

Micro-elemental analyses were performed using the Micro-elemental analytical facility. The micro-elemental analyses were used to ascertain the purity of the as-synthesised metal oleate precursors. The theoretical elemental percentages were compared to the experimental elemental percentages of the different elements in the precursors. The elements analysed were C and H. Potential errors could arise from the flow rate, heating rate, geometry among others.

2.8 Thermogravimetry Analysis (TGA)

Perkin Elmer TGA7 analyser was used to investigate the thermal behaviour of precursors. Each of the samples was heated from 25 to 600 ^oC under nitrogen atmosphere. The experimental decomposition percentages of metal oxide in each of the three samples were then compared to the theoretical decomposition of metal oxide in the three different precursors. One of the limitations in TGA analysis is that chemical changes which are not accompanied by the change in mass on heating are not indicated.

2.9 Synthesis of Fe_2O_3 nanoparticles from Iron oleate precursor

The precursors were subjected to heat treatment to decompose them to obtain nanoparticles. The reaction took place in a horizontal tube furnace reactor. The powder of Iron oleate precursor (0.20 g) was place in a ceramic boat which was then inserted into the centre of a quartz tube. The quartz tube was then placed inside the tube furnace with one end connected to the nitrogen gas flowing at the rate of 160 cubic centimetre per minute. The furnace was then heated for the different temperatures and times. The dark brown product obtained after the decomposition process was then collected and analysed. The same method was used to synthesis ZnO and CuO nanoparticles from their respective zinc oleate and copper oleate precursors.

2.10 Characterization of Fe_2O_3, ZnO and CuO nanoparticles

X-ray Diffraction (XRD) of Fe_2O_3, ZnO and CuO Nanoparticles Bruker D8 AXS diffractometer equipped with monochromatic Cu-Ka radiation was used for the XRD characterization. The samples were scanned between 20 and 85 degrees at a count rate of 10 s. The samples were prepared by dispersing the little amount of each of the metal oxide in hexane and spreading on a glass slide. The size of the crystallite D was calculated according to the Sherrer equation: $D = \frac{k\lambda}{bcos\theta}$

Where b is the full width at half maximum, λ is the wavelength of the radiation, θ is the angle of diffraction and k = 0.9 is the Scherrer constant. These are some of the limitations in XRD characterization technique; It cannot identify amorphous materials, no depth profile information and minimum spot size.

2.11 Transmission Electron Microscopy (TEM)

Sample treatment was done for TEM characterization by evaporating a hexane solution of the as- prepared nanoparticles of metal oxides on carbon coated copper grids. The micrographs of the nanoparticles were obtained by using a Philips CM200 Transmission Electron Microscope. The images were obtained at both low and high magnifications. The images obtained at high magnifications were used to determine the lattice fringes.

2.12 Fourier Transform-Infrared Spectroscopy (FT-IR)

The Perkin Elmer FT-IR spectrophotometer with Bruker detector was used to characterise the metal oxides nanoparticles. The metal oxide nanoparticles were scanned as solids from 4000–500 cm^{-1}. Wave numbers of the spectra were compared to literature to find out the functional groups present in each metal oxides nanoparticles synthesised.

3. Results and discussions

Fourier Transform Infra-Red (FTIR)of Metal Oleate Precursor. The functional groups in each of the three samples were identified using the FTIR spectroscopic method on the as-synthesized metal oleate precursors. Figure 1 depicts typical bands of interest.

The O-H functional group is represented by the absorption band at 3500 cm^{-1}. The presence of the O-H functional group on the surface of the copper oleate complex indicates the presence of moisture. In Sample A, the primary absorption bands are 2925 cm^{-1}, which corresponds to the vibrations of CH_2 in the oleate, 1713 cm^{-1} (C=0), 1574 cm^{-1} for C=C, 1443 cm^{-1} for C-O, 722 cm^{-1} (O-C=O), and 596 cm^{-1} for Cu-O, which are comparable to the findings in the literature (Pereira, 2012). Copper (II) oleate was found in Sample A. In sample B, the IR main bands are 2924 cm^{-1} for C-H, 1715 cm^{-1} for C=O, 1575 cm^{-1} for C=C, 1445 cm^{-1} for C-O, 722

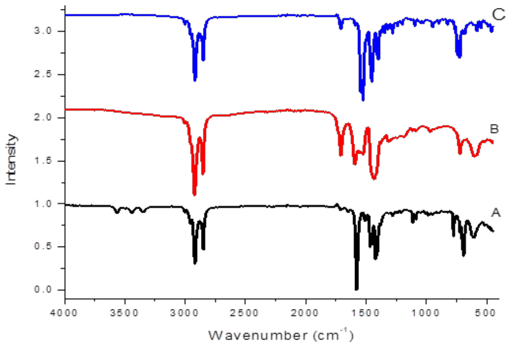

Figure 1. FT-IR spectra for metal oxide precursors; A: Copper oleate, B: Iron oleate and C: Zinc Oleate

cm^{-1} for O-C=O, and 588 cm^{-1} for O-C=O (Fe-O). Because the spectra revealed no O-H stretching mode, there were no water molecules in the Iron oleate complex. These iron oleate wave number values are comparable with what has been reported in the literature (Pereira, 2012; Zhanglei et al., 2012). Zinc oleate was discovered in Sample C. The large peak at 2924 cm^{-1} is attributed to CH2 vibrations in the oleate, with 1716 cm^{-1} for C=C, 1444 cm^{-1} for C-O, 722 cm^{-1} for O-C=O, and 667 cm^{-1} for Zn-O (Pereira, 2012; He and Tsuzuki, 2012).

3.1 Micro-elemental analysis of Copper, Iron and Zinc oleate precursors

Micro-elemental analysis was used to determine the purity of the copper, iron, and zinc oleates precursors. The relative makeup of each element in the complex is determined by this study. To assess the purity of the as-synthesised precursors, the predicted or theoretical elemental percentages are compared to the empirically obtained ones. The purity of the synthesised oleate complexes is determined by how near the experimentally determined value is to the predicted value. The copper, iron, and zinc oleates are quite pure when compared to the data in Table 1. Because all the samples were sticky and difficult to dry, the disparities in the readings may be ascribed to moisture.

Table 1. Micro-elemental analysis of copper, Iron and Zinc oleates

	Element	%Expected	%Found
Copper Oleate	C	69.02	65.48
	H	10.62	10.83
Iron Oleate	C	72.05	69.80
	H	11.06	11.17
Zinc Oleate	C	68.82	72.10
	H	10.59	11.64

3.2 Thermogravimetric analysis (TGA) of Copper, Iron and Zinc oleate precursors

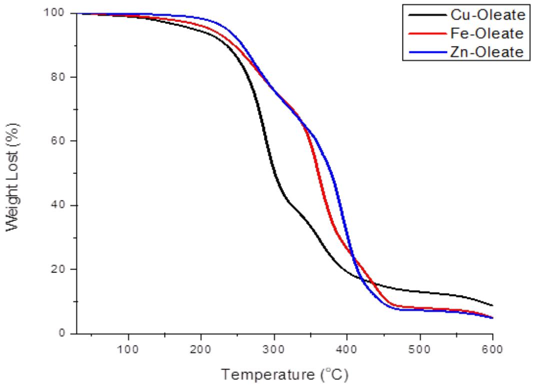

Figure 2. TGA of Copper, Iron and Zinc Oleate Precursors

As shown in Figure 2, the breakdown routes of the Zn-oleate, Fe-oleate, and Cu-oleate complexes were investigated in relation to the TGA spectra. The evaporation of the absorbed moisture may be responsible for the initial modest weight loss in each oleate complex at about 100 °C. The TGA curves of the Fe (III), Cu (II), and Zn (II)-oleate complexes are comparable to those seen in the literature (Marrow and Barron, 2015). There are two separate weight-loss protocols for the iron (III) complex. The first part (beginning at 160 °C) reflects the decomposition of a single oleate ligand from the complex, while the second (starting around 300 °C) represents the decomposition of the remaining two oleate ligands. The middle region of the graph, where the slope flattens, is attributed to the breakdown of oleate molecules that are weakly bound or even free, according to Marrow and Barron. Copper (II)-oleate has a TGA curve similar to iron (III)-oleate, although the temperatures associated with weight loss are significantly higher (240 °C and 400 °C, respectively), as well as slightly steeper weight loss rates. The loss of the oleate moiety in the complex might explain the substantial weight loss seen between 250 °C and 560 °C. When compared to iron and/or copper equivalents, the zinc (II)-oleate has a distinct TGA curve. Between 150 °C and 500 °C, there is just one continuous weight loss. However, at roughly 250 °C, a considerable reduction in Zn-oleate occurred and ended around 500 °C. The real weight decrease was 79%. In terms of the formula weight of zinc-oleate, if the organic component is fully removed and just ZnO remains, the mass loss is around 88% (ChenSha et al., 2008). Furthermore, there was a mass differential of around 8%, which was due to the capping supplied by some of the oleate moieties in zinc oxide.

3.3 X-ray Diffraction (XRD) of the as-synthesised CuO nanoparticles

The orientation and crystallinity of CuO nanoparticles degraded at 350 ^oC were revealed by the diffraction patterns. The locations of the peaks with 2 θ values of 31^o, 40^o, 47^o, 53^o, and 74.5^o are indexed (111), (111), (112), (020), (222), indicating the excellent crystalline nature of CuO with cubic symmetry (Rahman et al., 2009). CuO nanoparticles have a crystallite size of 8.2 nm, according to calculations. Impurities and other phases of copper oxide caused the peaks without the index (CuO). CuO nanoparticles have typically been synthesised using a combination of CuO and Cu2O nanoparticles (Yin et al., 2005; Rahman et al., 2009; Swarnkar et al., 2009).

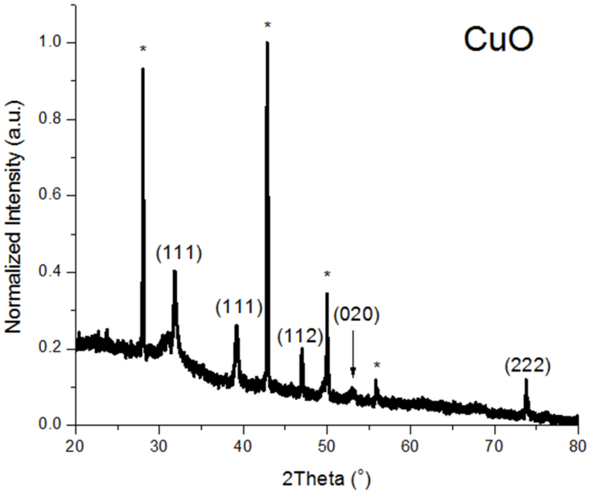

Figure 3. XRD of CuO nanoparticles obtained from the decomposition of copper oleate complex at 350 ^oC

3.4 X-ray Diffraction (XRD) of the as-prepared ZnO nanoparticles

XRD analysis after heating zinc oleate complex at 350 ^oC as shown in Figure 3. The peaks positions with 2θ values of 27^o, 28.5^o, 30^o and 43^o are indexed as (100), (002), (101) and (102) planes which are in good agreement with literature (Kulkarni and Shiras, 2015). The average crystallite size of the ZnO NPs was determined to be 11 nm with respect to Debye Sherrer equation. The remaining peaks without the index can be ascribed to the presence of other polymorphs of zinc oxide such as sphalerite, germanium phosphide (GeP) type among others.

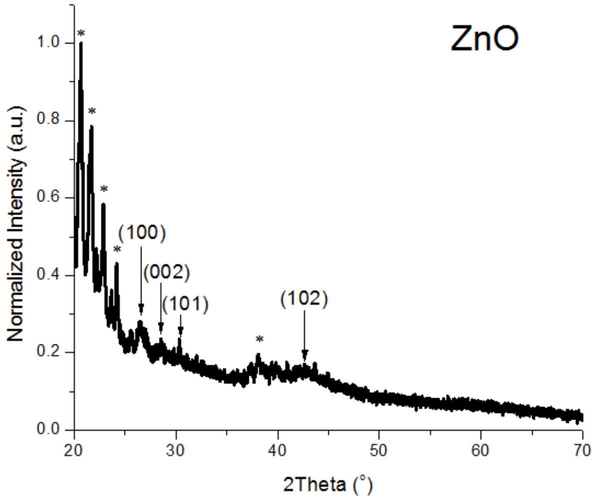

Figure 4. XRD of ZnO nanoparticles obtained from the decomposition of zinc oleate complex at 350 ^oC

3.5 X-ray Diffraction (XRD) of the as-synthesised Fe_2O_3 nanoparticles

Figure 4 shows an XRD pattern in iron oxide nanoparticles with $2\theta = 35$, 43, and 63. The planes (111), (200), and (220) are the peaks found in the angle. Peaks are identified by comparing them to published data. There were no additional phases found in the Fe_2O_3 nanoparticles that were produced. The hexagonal crystal unit cell of the nanoparticles was discovered (Saha and Bhunia, 2013). Using the Scherrer equation, the average crystallite size of the as-synthesised nanoparticles was found to be 16 nm.

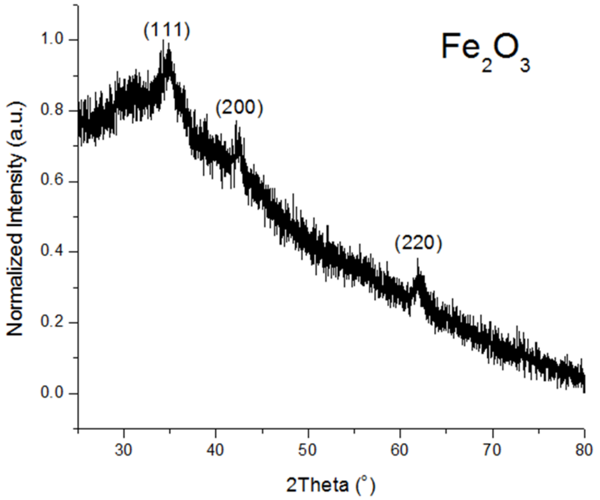

Figure 5. XRD of Fe_2O_3 nanoparticles obtained from the decomposition of iron oleate complex at 350 ^oC.

3.6 Transmission Electron Microscopy (TEM) of the as-synthesised CuO nanoparticles

The atomic structure of the material as well as any faults in the material may be determined using TEM. The TEM pictures reveal that CuO nanoparticles are crystalline, which is consistent with the XRD results. CuO nanoparticles vary in size from 8 to 25 nanometers, with an average nanoparticle size of 22 nanometers. The majority of the nanoparticles shown in (Figure 6) have cubic symmetry, with a few spherical and star forms.

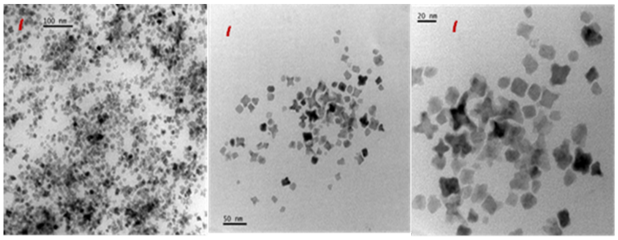

Figure 6. TEM of CuO nanoparticles

One of the potential errors in TEM analysis is that many samples are not stable under a high vacuum and high energy electron beam resulting in changes in the sample structure composition during imaging. In addition, the image diffraction pattern obtained is averaged through the thickness of the specimen.

3.7 FT-IR Spectra of Cu-Oleate precursor and CuO nanoparticles

The acquired spectra in (Figure 7) indicated that when the temperature rose from 250 to 400 ^oC, the peaks between 3300 and 2800 cm^{-1}, which represented the O-H functional group in the absorbed water as well as the C-H group, rapidly faded. At 400 ^oC, the O-H was entirely gone. CuO is represented by the peak at 640 cm^{-1}. Carbonyl C=O stretching vibrations are seen in the bands at 1585 and 1644 cm^{-1} in the spectra at 250 ^oC, 300 ^oC, and 350 ^oC (Dhineshbabu et al., 2015). Between 3300 and 2800 cm^{-1}, the C-H group in the oleate moeity stretching occurs. At temperatures between 250 and 350 ^oC, this is a sign of absorbed material on the surface of a nanoparticle.

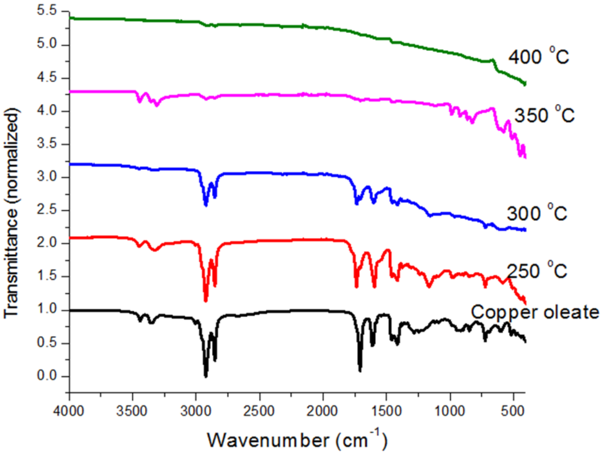

Figure 7. FT-IR spectra of copper oleate complex and the as-synthesised copper oxide nanoparticles at 250 ^oC, 300 ^oC, 350 ^oC and 400 ^oC.

3.8 FT-IR spectra of Zn-Oleate precursor and ZnO nanoparticles

The FT-IR curve for ZnO nanoparticles (Figure 8) demonstrated that breakdown of the zinc oleate precursor was unaffected by a temperature of 400 ^oC. As a result, breakdown of the precursor at temperatures higher than 400 ^oC would be necessary to get nanoparticles devoid of a large proportion of the organic moiety. When compared to the spectra of the original zinc oleate precursor, the spectra of the nanoparticles decomposed at 400 ^oC indicated certain structural alterations that may be attributed to the loss of some of the organic moiety in the as-synthesised nanoparticles (Awwad et al., 2014). The Zn-O bond is shown by the peak at 667 cm^{-1}. Furthermore, the peaks ranging from 800 to 1300 cm^{-1}, 1500 to 1700, 2300 to 2900 cm^{-1}, and 2300 to 2900 cm^{-1}, respectively, reflect C-C, C-O and C-H stretching modes. The presence of further oleate peaks in the spectra at 400 ^oC, with peak locations of 1089 and 888 cm^{-1}, suggests that the zinc oxide nanoparticles were encapsulated by the oleate molecule to avoid agglomeration (Rongliang and Tsuzuki, 2012). In all the spectra representing zinc oleate and the nanoparticles synthesised at temperatures of 250, 300, 350, and 400 ^oC, there were no peaks indicating the O-H stretching mode. This indicates that neither the precursor nor the zinc oxide nanoparticles absorbed water molecules.

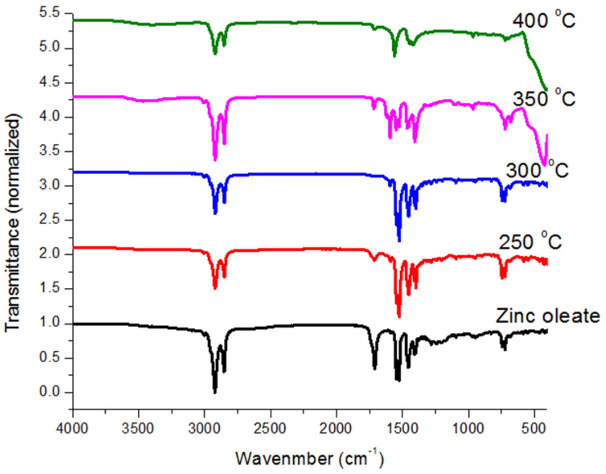

Figure 8. FT-IR spectra of zinc oleate complex and the as-synthesised zinc oxide nanoparticles at 250 ^oC, 300 ^oC, 350 ^oC and 400 ^oC.

3.9 FT-IR spectra of Fe-Oleate precursor and Fe_2O_3 nanoparticles

The FT-IR curve for Fe_2O_3 nanoparticles (Figure 9) revealed that a temperature of 400 ^oC had minimal effect on the precursor's breakdown. However, when the temperature increased from 250 °C to 400 °C, the intensity of the peaks decreased, suggesting that part of the oleate component had been lost. For full disintegration of the oleate complex to provide the requisite iron oxide nanoparticles, a temperature higher than 400 ^oC would be desirable. FeO stretching is responsible for the band at 462 and 560 cm^{-1} (Sahoo et al., 2010). Similarly, C-C stretching is responsible for the band at 800 – 1300 cm^{-1}. Furthermore, the antisymmetric and symmetric C-O and C-H stretching modes are represented by the absorption bands ranging from 1500 to 1700, 2300 to 2900 cm^{-1} respectively. In all the spectra of iron oxide nanoparticles, the peak indicating the O-H group was missing. This indicates that the nanoparticles as synthesised did not absorb water molecules and were hence exceedingly dry. The existence of C=O and C-C in the oleate may be attributed to the observed vibration bands in 1733 and 1300cm^{-1}, respectively. According to the FTIR results, oleic acid served as a capping agent, preventing aggregation (Mahdavi et al., 2013).

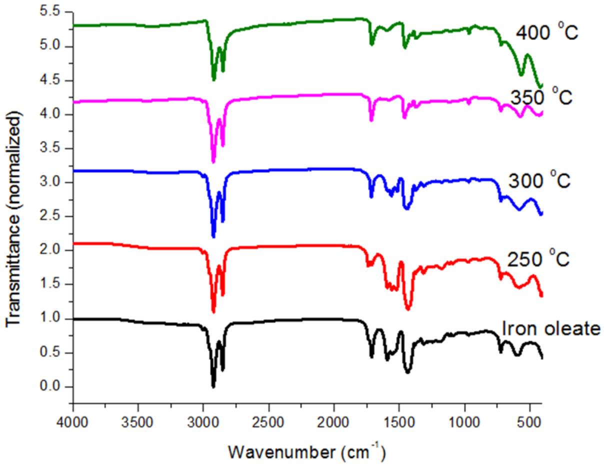

Figure 9. FT-IR spectra of iron oleate complex and the as-synthesised iron oxide nanoparticles at 250 ^oC, 300 ^oC, 350 ^oC and 400 ^oC.

3.10 Potential applications of ZnO, CuO and Fe_2O_3 nanoparticles

Owing to their distinct properties, nanoparticles made from organometallic complexes of the first transition metals family specifically, CuO, Fe_2O_3, and ZnO nanoparticles, offer a wide range of potential uses. Zinc oxide, for example, has a high refractive index, is non-toxic, has thermal conductivity, has anti-microbial properties, has UV protection, and has a broad band gap (3.37 eV). Zinc oxide nanoparticles have been found to be useful in solar cells, light emitters, piezoelectric transformers, optoelectronic devices, cosmetic and pharmaceutical products, chemical sensors, gas sensors, biosensors, varistors, field emitters, and the surface of acoustic-wavelike devices, among other applications (Janković et al., 2018). Similarly, copper (II) oxides with a band gap of 1.2 eV which is less toxic has also been used in catalysis, molecular adsorption, electro-conductive, optical materials, magnetic storage media, batteries, field emission, gas sensors, surfactants, and medical technology (Abbasi et al., 2018; Baqer et al., 2018; Wang et al., 2017). Iron oxide nanoparticles also have unique properties such as non-toxicity, biocompatibility, super magnetism among others and thus making them ideal candidates for many important applications. Due to their biocompatibility and super magnetic properties, they are used in molecular imaging, hyperthermia treatment, drug delivery, protein separation and many others (Lakshmanam Palanisamy et al., 2023). Moreover, they have been found useful in solar cells, catalysis, electronics, gas sensor and energy storage (Ayad & Ahmed, 2022).

4. Conclusion

This study used a solventless method to synthesize metal oxide nanoparticles, specifically iron (II) oxide NPs, copper (II) oxide NPs, and zinc oxide NPs, which were then characterized using a variety of traditional techniques including TGA, FT-IR, XRD, TEM, and micro-elemental analysis. The morphological characterizations of the produced CuO NP by TEM and XRD indicated that they were crystalline and closely matched the XRD pattern. CuO nanoparticles are 22 nm in size on average. Most of the nanoparticles seen in the micrograph had cubic symmetry. XRD for both ZnO and Fe_2O_3, showed crystallite diameters of 11nm and 16 nm, respectively.

References

[1] Abbasi Z, Salehi M, Khaleghian A, Kubicki M (2018) Co (III), V (IV) and Cu (II) complexes of bidentate N, O - donor Schiff base ligands: Characterization, anticancer activities and metal oxide nanoparticles preparation via solid state thermal decomposition. Appl organometallic chem. 1-11.

[2] Ajamein H, Haghighi M, Alaei S, Minaei, S (2017) Microporous and Mesoporous Materials Ammonium nitrate-enhanced microwave solution combustion fabrication of CuO / ZnO / Al 2 O 3 nanocatalyst for fuel cell grade hydrogen supply. Microporous and Mesoporous Materials, 245, 82–93. doi:10.1016/j.micromeso.2017.03.003.

[3] Awwad A, Albiss B, Almad A (2014) Green synthesis, characterization and optical properties of zinc oxide nanosheets using olea europea leaf extract. Adv. Mat. Lett. 5(9), pp. 520-524.

[4] Ayad MN., & Ahmed H (2022). An Overview of Iron Oxide Nanosparticles: Characterization, Synthesis and Potential Applications, Nanomaterial, Volume 20, issue 1, 145-158

[5] Baqer AA, Matori KA, Al-Hada NM, Shaari AH, Kamari HM, Saion E, Chyi JLY, Abdullah CAC (2018) Synthesis and characterization of of binary (CuO)0.6(CeO2)0.4 nanoparticles via a simple heat treatment method, Results in Physics,

[6] Barreca D, Gasparotto A, Maragno C, Seraglia R, Tondello E, Venzo A, Krishnan V (2005) Cadmium O-alkylxanthates as CVD precursors of CdS: a chemical characterization. Applied Organometallic Chemistry, 19(1), 59–67.

[7] Boles MA, Engel M, Talapin, DV (2016) Self-Assembly of Colloidal Nanocrystals: From Intricate Structures to Functional Materials. Chemical Reviews. American Chemical Society September 28, pp 11220–11289. https://doi.org/10.1021/acs.chemrev.6b00196.

[8] Chavali MS, Nikolova MP (2019) Metal oxide nanoparticles and their applications in nanotechnology. SN applied sciences, 1(6), 1-30.

[9] Chen CY, Wu SJ, Li JY, Wu CG, Chen JG, Ho KC (2007) A New Route to Enhance the Light Harvesting Capability of Ruthenium Complexes for Dye Sensitized Solar Cells. Advanced Materials 19, pp. 3888–389.

[10] Chensha LI, Yuning LI, Yiliang WU, Ong S, Loutfy RO (2008) Synthesis of zinc oxide nanocrystals by thermal decomposition of Zn-oleate in organic medium. 51(12), pp.2075–2079.

[11] Christia C and Bogdan SV (2020) New Approaches in Synthesis and Characterization Methods of Iron Oxide Nanoparticles DOI: http://dx.doi.org/10.5772/intechopen.101784

[12] Dhineshbabu NR, Vetumperumal VRNNR (2015) Study of structural and optical properties of cupric oxide nanoparticles. Applied Nanoscience, (Greenwood 2003). Available at: "http://dx.doi.org/10.1007/s13204-015-0499-2

[13] Duan T, Lou W, Wang X, Xue Q (2007) Size-controlled synthesis of orderly organized cube-shaped lead sulfide nanocrystals via a solvothermal single-source precursor method. Psysicochemical Engineering Aspects, 310, pp. 86–93.

[14] Droepenu EK, Boon SW, Suk, FC Kuan, YK Muhammad, FM (2021). Zinc Oxide Nanoparticles Synthesis Methods and its Effect on Morphology: A Review, Journal of Biointerface Research in Applied Chemistry , Volume 12, Issue3,2022, 4261-4292

[15] Fan D, Afzaal M, Mallik MA, Nguyen CQ, O'Brien P, Thomas J (2007). Using coordination chemistry to develop new routes to semiconductor and other materials. Coordination Chemistry Reviews, 251(13-14), pp. 1878–1888.

[16] George JM, Antony A, Mathew B. (2018) Metal oxide nanoparticles in electrochemical sensing and biosensing: a review. Microchimica Acta, 185(7), 1-26.

[17] He R, Hocking RK, Tsuzuki T (2012) Local structure and photocatalytic property of sol–gel synthesized ZnO doped with transition metal oxides. J Mater Sci 47, 3150–3158 https://doi.org/10.1007/s10853-011-6149-5

[18] Jankovi S, Milisavi D, Okoli T, Jeli D (2018) Preparation and Characterization of ZnO Nanoparticles by Solvent Free Method, 1, 48–52. doi:10.7251/COMEN1801048J.

[19] Kulkarni SS (2015) Optical and Structural Properties of Zinc Oxide Nanoparticles. 2(1), pp.14–18.

[20] Lakshmanam Palanisamy, K., Vignesh, K., & Karthikeyan, N. (2023). Applications and Toxicology of iron oxide Nanoparticles. IntechOpen. Doi: 10.5772/intechopen.1001336

[21] Liu B, Zeng HC (2003) Journal American Chem. Soc., pp. 125: 4430.

[22] Mahdavi M, Namvar F, Ahmad M, Mohamad R (2013) Green Biosynthesis and Characterization of Magnetic Iron Oxide (Fe3O4) Nanoparticles Using Seaweed (Sargassum muticum) Aqueous Extract, 5954–5964. doi:10.3390/molecules18055954.

[23] Morrow L, Barron AR (2015) Issues Affecting the Synthetic Scalability of Ternary Metal Ferrite Nanoparticles. Vol., 2015, pp.1–9.

[24] Niloufar AT, Abouzar T (2019) Synthesis and characterization of copper oxide nanocrystal via preparation of precursor tri-homonuclear inorganic complex, Inorganic and Nano-Metal Chemistry, 49:4, 107-112, DOI: 10.1080/24701556.2019.1606826.

[25] Panchakarla LS, Shah MA, Govind Raj A, Rao CNR (2007) J. Solid Stat Chem., 180: 11 3106.

[26] Pereira AS, Silva NJO, Trindade T, Pereira S (2012) A Single-Source Route for the Synthesis of Metal Oxide Nanoparticles Using Vegetable Oil Solvents. , 12(xx), pp.1–6.

[27] Rahman A, Ismail A, Jumbianti D, Magdalena S, Sudrajat H (2009) Synthesis of copper oxide nanoparticles by using Phormidium cyanobacterium. Indo J Chem 9: pp.355–360.

[28] Ritch JS, Chivers T, Ahmad K, Afzaal M, O'Brien P (2010) Synthesis, structures, and multinuclear NMR spectra of tin(II) and lead(II) complexes of tellurium-containing imidodiphosphinate ligands: preparation of two morphologies of phase-pure PbTe from a single-source precursor. Inorganic Chemistry, 49(3), pp. 1198–2005.

[29] Rongliang H, Rosalie K, Hocking, Takuya T (2012) Co-doped ZnO nanopowders: Location of cobalt and reduction in photocatalytic activity, Materials Chemistry and Physics, Volume 132, Issues 2–3, Pages 1035-1040,

[30] Saha S, Bhunia AK, (2013) Synthesis of Fe2O3 Nanoparticles and Study of its Structural, Optical Properties. , 17(December), pp.191–195.

[31] Sahoo NG, Rana S, Cho JW et al. (2010). Polymer Nanocomposites Based on Functionalized Carbon Nanotubes. Progress in Polymer Science, 35, 837-867.

[32] Sharma P, Pant S, Dave V, Tak K, Sadhu V (2019) Green synthesis and characterization of copper nanoparticles by Tinospora cardifolia to produce nature-friendly copper nano-coated fabric and their antimicrobial evaluation. Journal of Microbiological Methods, 160(January), 107–116. doi:10.1016/j.mimet.2019.03.007.

[33] Singhal A, Dutta DP, Tyagi AK, Mobin SM, Mathur P, Lieberwirth I (2007) Palladium (II)/allylpalladium(II) complexes with xanthate ligands: Singlesource Precursors for the generation of palladium sulfide nanocrystals. Journal of Organometallic Chemistry, 692(23), pp.5285–5294.

[34] Swarnkar RK, Singh SC, Gopal R (2009) Optical characterizations of copper oxide nanomaterial. In: Proceedings of the ICOP International Conference on Optics and photonics. CSIO, Chandigarh

[35] Wang Q, Zhang Y, Zheng J, Wang Y, Hu T, Meng C (2017) Metal oxide decorated layered silicate magadiite for enhanced properties: insight from ZnO and CuO decoration 4303–4316. doi:10.1039/c7dt00228a.

[36] Yin M, Wu CK, Lou Y, Burda C, Koberstein JT, Zhu Y, O'Brien S (2005) Copper oxide nanocrystals. J. Am. Chem. Soc., 127, pp. 9506–9511.

[37] Yin M, Wu CK, Lou Y, Burda C, Koberstein JT, Zhu Y, O'Brien, S (2005). Copper oxide nanocrystals. J. Am. Chem. Soc., 127, pp. 9506–9511.

[38] Zhanglei N, Zhidong C, Wenjun LI (2012) Solvothermal Synthesis and Optical Performance of One-dimensional Strontium Hydroxyapatite Nanorod , 20(1), pp.89–94.

[39] Zhao N, Osedach TP, Chang LY, Geyer SM, Wanger D, Binda MT, Arango AC, Bawendi MG, Bulovic V (2010) Colloidal PbS Quantum Dot Solar Cells with High Fill Factor. ACS Nano 4, pp. 3743–3752.